Impact of Virtual Admittance-Based Grid-Forming Control on Distance Protection

Shipra Tiwari, Adrian W. Diaz Sarmiento, Jose Pissolato Filho, and F. B. Costa .

***Abstract*—This paper examines the impact of GFM inverter utilizing virtual admittance loop control on the apparent impedance measured at relays protecting a transmission line connected to a strong grid. A detailed electromagnetic transient model is used to analyze internal and external faults under various virtual impedance values. A dq domain analysis of current response is performed to interpret the active and reactive current contributions that shape the apparent impedance trajectory. For single-phase-to-ground faults, the distance element operates correctly. However, for three-phase, phase-to-phase, and phase-to-phase-to-ground faults, the inverter control causes significant deviation in the apparent impedance, resulting in misopertion at the inverter-side relay. Increasing the virtual impedance improves security for some cases but does not fully restore correct operation. These results indicate that conventional distance protection requires adaptation in GFM-dominated networks.**

***Index Terms*—Grid-forming, distance protection, virtual admittance, inverter-based resources.**

I. Introduction

The increasing penetration of inverter-based resources (IBRs) is accelerating the transition toward power systems with reduced synchronous machine support. Among these, grid-forming (GFM) inverters have attracted significant attention for their ability to establish voltage and frequency references, thereby ensuring stable operation in weak-grid and low-inertia environments [1]. This contrasts with grid-following (GFL) inverters, which depend on external grid conditions for synchronization [2]. While GFL fault ride-through (FRT) strategies focus on shaping current characteristics, GFM FRT schemes prioritize maintaining voltage-source behavior and enforcing proper current limitation during faults [2]. Consequently, the fault current waveform of GFM-based IBRs differs markedly from that of GFL inverters. Among various limitation strategies, magnitude-based circular current limiting has gained increasing adoption because it constrains current magnitude while preserving its vector angle, effectively modifying the inverter's output impedance in real time [3]. This approach enables smooth recovery to normal operation after fault clearance and ensures stable fault current control.

The effect of IBRs on conventional protection schemes has been widely studied in the literature [4]–[7], but most work has focused on GFL inverters. Given the fundamentally different FRT behavior of GFM units, an investigation into their impact on distance protection is required. Distance relays operate by estimating the apparent impedance (Z_{AP}) from local voltage and current measurements to determine whether a fault lies within the protected line section. When a GFM inverter dynamically adjusts its virtual impedance (Z_v) during fault conditions, the voltage–current relationship observed by the relay no longer reflects the physical line impedance. As a result, the Z_{AP} trajectory may shift significantly, causing overreach, underreach, or misoperation [8]. Prior work mainly focused either on the reliability of supervising elements under various GFM current limiting strategies [3], or on fault loop impedance estimation under a limited set of GFM control architectures and LL faults [9]. Others examine distance element performance based on X and M calculations for commercial relays, but with fixed GFM settings [10]. However, these studies did not examine how active-reactive current behavior, circular current limiting, virtual admittance variation, and fast GFM transients influence the apparent impedance trajectory for internal and external faults.

This paper fills these gaps by systematically analyzing different faults, varying the virtual admittance, and linking the inverter control dynamics and saturation behavior to the observed deviation of impedance trajectory across the protection zones. The circular current limiter is employed in a GFM inverter to maintain a constant dq current angle. Additionally, the inverter's fault current response is analyzed in the dq reference frame to link active and reactive current dynamics directly to the apparent impedance trajectory. The results demonstrate that Z_v significantly alters the measured impedance path, particularly for line-to-line and double-line-to-ground faults, where relay misoperations are more likely. These findings emphasize that virtual impedance tuning, current-limiting dynamics, and relay setting coordination jointly determine the dependability of protection in networks with high GFM penetration.

II. System Description

The system under study is shown in Fig. 1. It consists of a GFM inverter connected through a 38.5/400 kV transformer to a 50 Hz transmission system, with two parallel conventional sources connected at Bus 3 through transmission lines of 120 and 110 km. The transmission lines are modeled using a π-equivalent representation with positive- and zero-sequence impuissances of $Z_L^+ = 0.0357 + j\,0.5077\ \Omega/\text{km}$ and $Z_L^0 = 0.3630 + j\,1.3262\ \Omega/\text{km}$, respectively. The

Shipra Tiwari and F. B. Costa are with the Department of Electrical and Computer Engineering, Michigan Technological University, Houghton, United States of America (e-mail: shiprat@mtu.edu, fbcosta@mtu.edu) Adrian W. Diaz Sarmiento and Jose Pissolato are with the Department of Electrical and Computer Engineering, University of Campinas, Campinas 13083-852, Brazil (e-mail: a196151@dac.unicamp.br, pisso@unicamp.br).

979-8-3315-8138-1

voltage sources are characterized by different phase angles and equivalent sequence impedances: Source 1 has $\underline{V}_{s1} = 400\,\text{kV}\angle-2.0^\circ$, $Z_{s1}^{+} = 7.76\angle 86^\circ\ \Omega$, and $Z_{s1}^{0} = 5.00\angle 86^\circ\ \Omega$, while Source 2 has $\underline{V}_{s2} = 400\,\text{kV}\angle-6.9^\circ$, $Z_{s2}^{+} = 12.7\angle 82^\circ\ \Omega$, and $Z_{s2}^{0} = 11.2\angle 82^\circ\ \Omega$. The synchronous generators (SGs) are modeled as an equivalent three phase voltage source. This simplification is valid for short-duration fault studies, as the generator electromechanical and excitation dynamics are much slower than the fast inverter control actions considered in this paper. The point of common coupling (PCC) serves as the measurement location for voltage and current, which are transformed into the dq reference frame for control and analysis. The GFM control strategy generates the power angle reference δ_{gfm} and frequency reference ω_{gfm} using active power droop control (the P–ω loop). The reactive power–voltage control (Q–V loop) provides the internal voltage reference for the inverter voltage regulator. A virtual admittance network, defined by the virtual inductance L_{eq} and resistance R_{eq}, produces the unconstrained current references $I_{d,UL}$ and $I_{q,UL}$. Since the inverter has a maximum allowable current limit $I_{\max}$, a circular current-limiting strategy is applied to obtain the constrained currents $I_{d,L}$ and $I_{q,L}$. Finally, a conventional current control stage generates the inverter output voltage for the averaged model implementation. The averaged model is adopted in this work because it reduces computational burden and remains accurate for the low-frequency dynamics of interest [11].

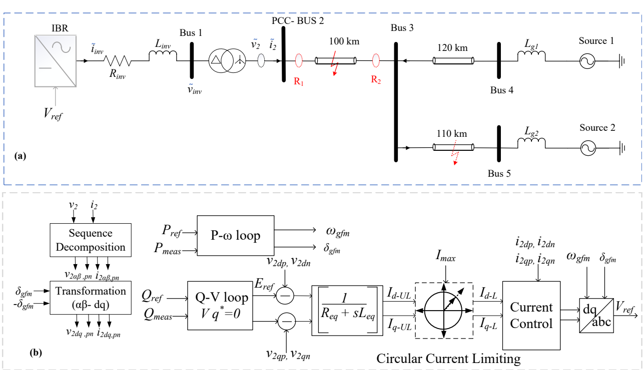

Fig. 1. Configuration of GFM-based IBR power system under study (a) Main circuit (b) Control structure

Varying the Z_v directly influences whether the current-limiting algorithm becomes active. As Z_v increases, the inverter exhibits a higher effective output impedance, thereby reducing the fault current contribution. Consequently, for sufficiently large Z_v, the inverter current may remain below the maximum allowable current I_{max}, and the circular current limiter does not activate.

A. Control Strategy

Reactive Power Control (Q–V Loop): The Q–V loop generates the internal voltage magnitude reference E_{ref} [3]:

$$E_{ref} = \int k_i\left[(V_N - V_{2d})k_q + (Q_{ref} - Q_{meas})\right] dt + V_{pre}, \quad (1)$$

where k_i and k_q are PI gains, V_N and Q_{ref} are the nominal voltage and reactive power reference, Q_{meas} is the measured reactive power, V_{2d} is the positive-sequence d-axis PCC voltage, and V_{pre} is the pre-fault voltage. The output of this loop is constrained to 1 p.u.

Active Power Control (P–ω Loop): This loop generates the power angle reference δ_{gfm} [3]:

$$\delta_{gfm} = \int \frac{(P_{ref} - P_{meas})}{2H}\, dt + k_{pd}(P_{ref} - P_{meas}), \quad (2)$$

where P_{ref} and P_{meas} are the reference and measured active powers, H is the inertia constant, and k_{pd} is the damping coefficient.

Virtual Admittance Loop: The unlimited dq current references I_{dq-UL} are generated using the virtual admittance loop [12], given as:

$$I_{d-UL} = \frac{1}{Z_v}(E_{ref} - V_d); \quad I_{q-UL} = \frac{1}{Z_v}(-V_q), \quad (3)$$

where $Z_v = R_{eq} + j\omega L_{eq} = (R_{inv} + R_v) + j\omega(L_{inv} + L_v)$.

The inverter filter and virtual resistance and inductance are denoted as R_{inv}, L_{inv}, R_v, L_v, respectively.

Circular Current Limiter: The limited current through circular limiter is given if $|I_{dq,UL}| > I_{max}$ [12],

$$I_{dq,L} = I_{dq,UL} \cdot \frac{I_{max}}{|I_{dq,UL}|}. \quad (4)$$

Inner Current Control Loop: A standard PI current controller generates the inverter modulation signals for the averaged model implementation [11].

The IBR's control parameters are presented in Table II.

III. Distance Protection Algorithm

Fig. 1 shows relays R_1 and R_2 located at both terminals of the transmission line connecting the IBR. They utilize distance protection logic that estimates the fault location by measuring the apparent impedance seen from the relay terminal, expressed as $Z_{AP} = V_{loop}/I_{loop}$, where the voltage and current depend on the fault loop specified in Table I. The loop is determined by identifying faulted phases following the traditional algorithm [13]. For phase-to-ground faults, zero-sequence compensation ($k \cdot 3I_0$) accounts for ground return effects, where $k = (Z_0 - Z_1)/3Z_1$ [13].

TABLE I
Loop Impedance Calculation Used in Distance Protection

Fault loop	Voltage Loop	Current Loop
Phase-to-ground	$V_{\phi 1}$	$I_{\phi 1} + k\,3I_0$
Phase-to-Phase	$V_{\phi_1} - V_{\phi_2}$	$I_{\phi_1} - I_{\phi_2}$

IV. Performance Analysis

The transmission system shown in Fig. 1 is used to evaluate the impact of varying Z_v on distance protection performance. Internal and external fault scenarios are simulated, including single-line-to-ground (SLG), three-phase-to-ground (3ϕ), line-to-line (LL), and double-line-to-ground

979-8-3315-8138-1

TABLE II
GFM INVERTER'S PARAMETERS USED IN THE ANALYSIS

Parameter	Value
Inertia Constant, H	2.5 s
Reference active power, P_{ref}	0.5 pu
Reactive power reference, Q_{ref}	0 pu
Equivalent resistance, R_{eq}	0.15 pu
Equivalent inductance, L_{eq}	0.5 pu
Maximum inverter current, $I_{\max}$	1 pu
Damping coefficient, K_{pd}	20 pu
Nominal voltage, V_N	1 pu
Reactive power loop integral gain, k_i	1
Reactive power loop proportional gain, k_q	0.1
Inner current loop proportional gain	1.25
Inner current loop integral gain	2.48

(2LG) faults. Three virtual-impedance settings are considered, low ($Z_v = 0.3$ pu), intermediate ($Z_v = 0.8$ pu), and high ($Z_v = 1.0$ pu), representing different levels of current saturation in the GFM-IBR during disturbances. The distance protection was configured with Zone 1 and Zone 2 reaches of 80% and 120%, respectively, and a fault-resistance reach of 100 Ω was applied across all cases for consistency.

A. Internal Faults

Fig. 2 shows the Z_{AP} trajectories measured by R1 for different internal fault types with $Z_v = 0.8$ pu. All ground-involved faults are simulated with a ground resistance of $1\,\Omega$. From the inverter side, only the SLG and 3ϕ faults fully enter Zone 1, allowing the distance element to operate. The 3ϕ fault trajectory, however, lies close to the Zone 1 boundary, indicating a limited security margin. For the LL and 2LG faults, the Z_{AP} trajectories momentarily cross into Zone 1 during the transient interval but subsequently settle outside the operating region. Consequently, the distance protection at R1 does not issue a trip for these fault types.

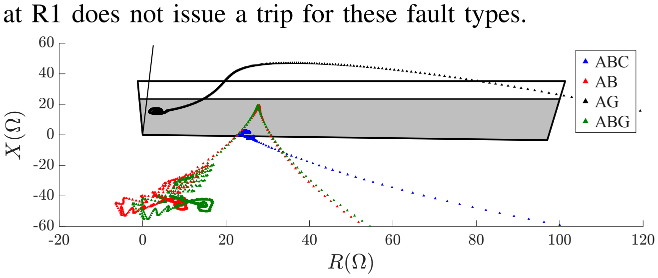

Fig. 2. Z_{AP} calculated by R1 during internal faults with $Z_v = 0.8$ p.u.

Fig. 3 shows the corresponding Z_{AP} trajectories seen by R2, located at the grid side when $Z_v = 0.8$ pu. In this case, all fault types fall correctly within the intended operating zones, and the distance protection operates as expected. This indicates that the grid provides a dominant infeed, resulting in more stable and reliable impedance estimation.

B. External Faults

For all external faults, the fault is applied 5 km from Bus 3 on the 110 km transmission line considering $Z_v = 0.8$ pu. Fig. 4 shows the Z_{AP} trajectories measured by relay R1. For the 3ϕ and SLG faults, the apparent impedance falls within

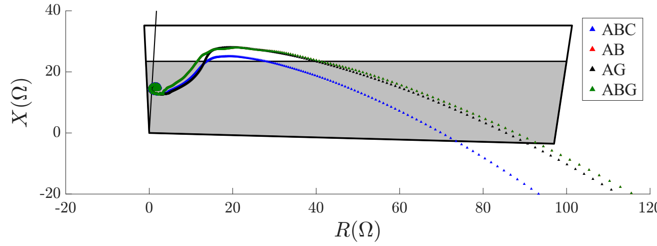

Fig. 3. Z_{AP} calculated by R2 during internal faults with $Z_v = 0.8$ p.u.

Zone 2 of the distance protection characteristic, which is the correct behavior for a fault located near the remote terminal on the adjacent line section. Conversely, for the LL and 2LG faults, the trajectories briefly cross into Zone 1 during the transient interval before settling outside the operating region. Since their steady-state impedance lies outside both Zone 1 and Zone 2, relay R1 correctly restrains and does not issue an operation for these faults.

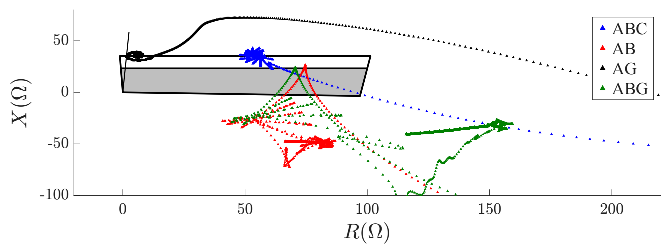

Fig. 4. Z_{AP} calculated by R1 during external faults with $Z_v = 0.8$ p.u.

Fig. 5 shows the performance of R2 for the same external fault conditions. All external faults appear as reverse faults. Therefore, all impedance trajectories fall outside the forward-operating characteristic, and the relay correctly restrains for all fault types. This confirms that the distance protection remains selective and secure from the grid side busbar.

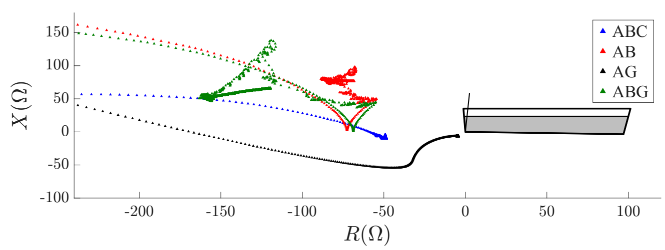

Fig. 5. Z_{AP} calculated by R2 during external faults with $Z_v = 0.8$ p.u.

C. Impact of the Virtual Impedance

1) Internal 3ϕ faults: Fig. 6 shows the effect of varying Z_v (0.4, 0.8, and 1.0 p.u.) on Z_{AP}, these values represent different systems strength at the POI when $R_f = 1\,\Omega$. For comparison, the trajectories obtained when a strong SG is connected at the point of common coupling instead of the IBR are also included. When $Z_v = 0.4$ p.u., the Z_{AP} falls clearly within Zone 1, resulting in correct operation of the distance element. For $Z_v = 0.8$ pu, the Z_{AP} trajectories remain within Zone 1 but lie close to its boundary. When $Z_v = 1.0$ pu, the Z_{AP} locus shifts outside the protection characteristic, causing the distance relay to misoperate. In contrast, when the source is a strong SG, the same 3ϕ faults with $R_f = 1\ \Omega$ and $10\ \Omega$ remain well inside Zone 1, demonstrating the reduced sensitivity of GFM-IBRs to distance protection due to the influence of virtual impedance.

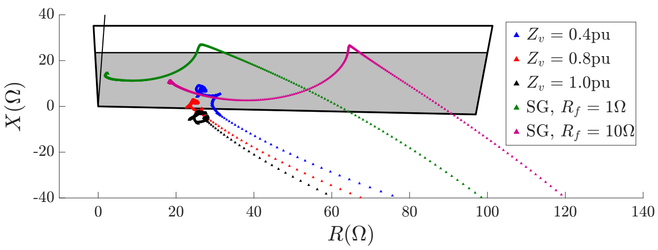

Fig. 6. Z_{AP} calculated by R1 for 3ϕ internal faults

2) Internal LL faults: Fig. 7 shows the impact of varying Z_v for LL faults. In this case, the main effect of Z_v is seen in the shape and evolution of the Z_{AP} trajectory during the transient period. Unlike the SLG case, the steady-state Z_{AP} shifts noticeably as Z_v changes. However, it remains outside any operating zone, so the distance element does not trip in any case. When compared with the SG case, the IBR exhibits a distinctly different transient impedance path, reflecting the influence of converter control dynamics on the behavior of LL faults.

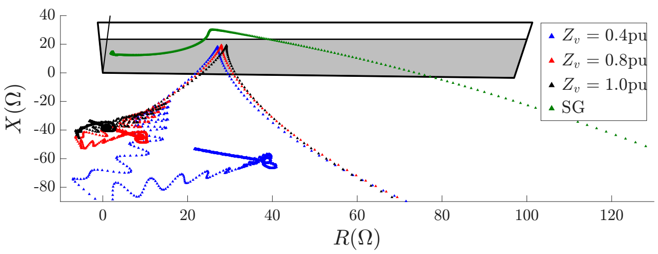

Fig. 7. Z_{AP} calculated by R1 for LL internal faults

D. Impact of R_f during faults

1) 3ϕ faults: 3ϕ faults were simulated for both internal and external locations, considering fault resistances of $R_f = 1\ \Omega$ and $R_f = 10\ \Omega$ with $Z_v = 0.8$ pu. As shown in Fig. 8, increasing R_f shifts the Z_{AP} locus toward the resistive axis, moving it outside the protection zone. This incorrect non-operation occurs even for $R_f = 10\ \Omega$, which does not constitute a high-resistance fault and should still be detected by the distance relay.

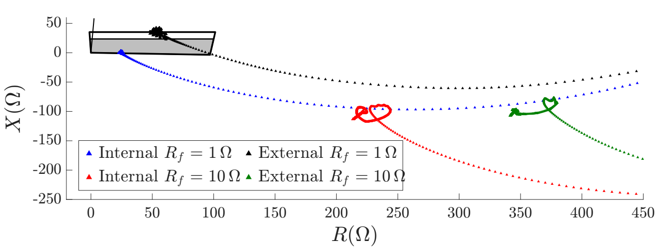

Fig. 8. Internal and external 3ϕ faults for $R_f = 1\ \Omega$ and $10\ \Omega$

Figs. 9 and 10 show the corresponding I_{dp} and I_{qp} waveforms for $R_f = 1\ \Omega$ and $10\ \Omega$. During internal faults, a low R_f produces a severe voltage drop, leading to strong current saturation and dominant reactive current injection (I_{qp}) that supports voltage recovery. The active current (I_{dp}) remains limited under these conditions. For external faults, a similar trend is observed, with I_{qp} approaching its saturation limit as the inverter injects reactive current to sustain voltage at the PCC. When R_f increases to $10\ \Omega$, the voltage drop is less severe, and the I_{dp} contribution remains close to its pre-fault value. For external faults, an even higher I_{dp} delivery is observed due to the increased effective impedance seen from the inverter terminal. The predominance of reactive current shifts the Z_{AP} locus upward along the imaginary axis, whereas greater active current contribution at higher R_f moves it rightward. These variations in the dq currents directly shape the apparent impedance trajectory observed during internal and external faults, explaining the distortion of Z_{AP} as fault resistance increases, ultimately hindering the correct operation of the distance protection.

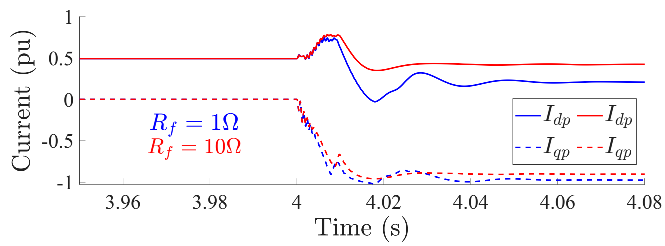

Fig. 9. I_{dp}, I_{qp} with Z_v=0.8 pu for 3ϕ internal faults, R_f= 1, 10 Ω.

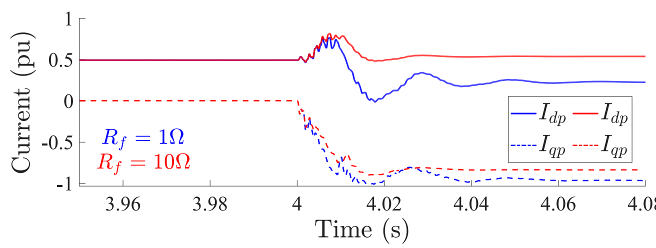

Fig. 10. I_{dp}, I_{qp} with Z_v=0.8 pu for 3ϕ external faults, R_f= 1, 10 Ω.

2) LL faults: LL faults were simulated for both internal and external locations, considering fault resistances of $R_f = 1\ \Omega$ and $R_f = 10\ \Omega$ with $Z_v = 0.8$ pu. As shown in Fig. 11, in all cases Z_{AP} remains outside the protection operating zones causing the relay to misoperate. The trajectories for internal and external faults exhibit a similar pattern, indicating that the inverter's current control response dominates.

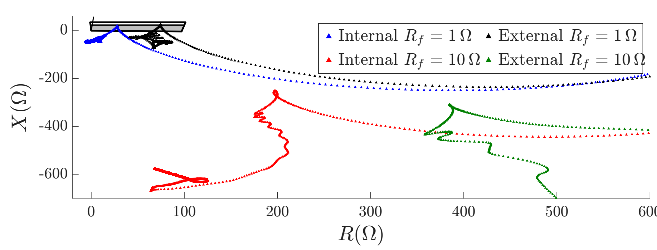

Fig. 11. Internal and external AB faults for $R_f = 1,\ 10\ \ \Omega$

Figs. 12 and 13 illustrate the corresponding dq current behavior for an internal LL fault with $R_f = 1\ \Omega$. The d component negative sequence current delivery deteriorates the trajectory, which alters the overall trajectory of Z_{AP} and drives it away from the protection zone. This effect is consistent with the inverter's control response under unbalanced conditions, where voltage support is primarily achieved through positive-sequence reactive current injection, while the positive d-component current decreases. The results confirm that the reactive component (I_{qp}) dominates to maintain voltage support, whereas the active component (I_{dp}) remains small. Similarly, the negative-sequence components (I_{dn}, I_{qn}) exhibit asymmetrical magnitudes that contribute to the distortion of the Z_{AP} locus. These interactions explain the consistent non-operation of the relay under LL fault conditions.

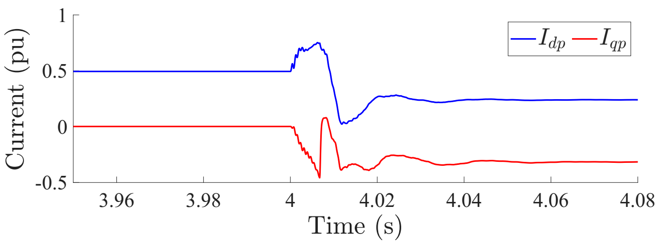

Fig. 12. I_{dp}, I_{qp} with Z_v=0.8 pu for AB internal faults, R_f= 1 Ω.

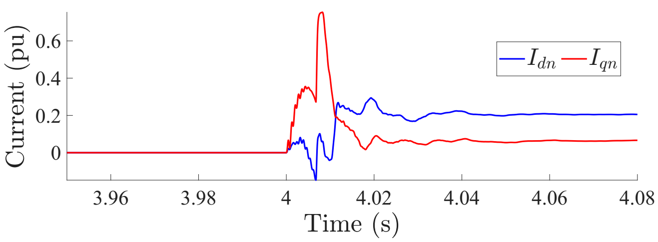

Fig. 13. I_{dn}, I_{qn} with Z_v=0.8 pu for AB internal faults, R_f= 1 Ω.

E. Final Discussion

The analysis shows that the apparent impedance trajectory for LL, 2LG, and 3ϕ faults with R_f of 10 Ω or more often remains outside the protection zones when a line is connected to a GFM-IBR. This protection behavior was observed in other system configurations using the same control strategy. Although 2LG faults were not shown due to space constraints, their behavior was similar to the LL fault. Under circular current saturation in the virtual impedance-based GFM-IBR, the current magnitude is limited, but its phase angle and active–reactive prioritization are not controlled, resulting in unsuppressed negative-sequence d-component current (I_{dn}) that distorts Z_{AP} in the LL and 2LG faults. Higher Z_v in the GFM-IBR control further weakens the grid, resulting in larger voltage deviations and increased current oscillations. Overall, the current distribution trend, fault sensitivity, and impedance trajectory displacement remain affected.

V. Conclusions

This paper evaluated distance protection performance in transmission lines connected to grid-forming inverters (GFMs) using a virtual admittance loop with current saturation control. Single-line-to-ground faults were correctly detected under all conditions, while three-phase faults became marginal or undetected when the inverter acted as a weak source, although higher virtual impedance improved security margins. For line-to-line and double-line-to-ground faults, the apparent impedance remained outside the tripping region regardless of the virtual impedance, due to the modified voltage–current relationship imposed by inverter control. The relay at the grid side remained reliable for all cases. A dq-domain analysis showed that reactive current dominance due to the voltage difference between the grid and the inverter, in order to support voltage, shifts the apparent impedance downward along the negative X-axis. While the active current contribution based on fault severity, location, and current limitation shifts the trajectory rightward along the R-axis. Unbalanced sequence interactions further distort the apparent impedance, confirming that misoperations stem from current saturation behavior and virtual impedance tuning, highlighting the need to adapt distance protection for GFM-based systems.

Acknowledgments

This paper was partially supported by the NSF under Grant No. 2501861 and by the FAPESP under Grants 2021/11258-5, 2023/15636-0, and 2025/03054-1.

References

[1] B. Bahrani, M. H. Ravanji, B. Kroposki, D. Ramasubramanian, X. Guillaud, T. Prevost, and N.-A. Cutululis, “Grid-forming inverter-based resource research landscape: Understanding the key assets for renewable-rich power systems,” *IEEE Power & Energy Magazine*, vol. 22, no. 2, p. 18–29, 2024.

[2] E. Farantatos, A. Banaie, A. Haddadi, and D. Ramasubramanian, “Fault-ride through performance analysis of grid-forming inverter-based resources,” Electric Power Research Institute (EPRI), Palo Alto, CA, Technical Report 3002029578, Apr. 2024.

[3] Y. Li, H. Wu, and X. Wang, “Impact of grid-forming inverters on protective relays: A perspective for current limiting control design,” *arXiv preprint arXiv:2505.04177*, 2025.

[4] A. Hooshyar, M. A. Azzouz, and E. F. El-Saadany, “Distance protection of lines emanating from full-scale converter-interfaced renewable energy power plants—Part I: Problem statement,” *IEEE Transactions on Power Delivery*, vol. 30, no. 4, pp. 1770–1780, 2015.

[5] Y. Fang, K. Jia, Z. Yang, Y. Li, and T. Bi, “Impact of inverter-interfaced renewable energy generators on distance protection and an improved scheme,” *IEEE Transactions on Industrial Electronics*, vol. 66, no. 9, pp. 7078–7088, 2019.

[6] A. Banaiemoqadam, A. Azizi, A. Hooshyar, M. G. Kanabar, and E. F. El-Saadany, “Impact of inverter-based resources on different implementation methods for distance relays—Part I: Phase comparators,” *IEEE Transactions on Power Delivery*, vol. 38, no. 6, pp. 4090–4102, 2023.

[7] J. Loebel and J. Jaeger, “Analytical investigation of influence of grid following IBR control on distance protection,” in *IET Conference Proceedings CP916*, vol. 2025, no. 5. IET, 2025, pp. 147–154.

[8] H. Johansson, Q. Xing, N. Taylor, and X. Wang, “Impacts of grid-forming inverters on distance protection,” *IET Generation, Transmission & Distribution*, vol. 19, no. 1, p. e13354, 2025.

[9] N. Baeckeland, D. Venkatramanan, S. Dhople, and M. Kleemann, “On the distance protection of power grids dominated by grid-forming inverters,” in *2022 IEEE PES Innovative Smart Grid Technologies Conference Europe (ISGT-Europe)*, 2022, pp. 1–6.

[10] C. L. Peralta and H. N. V. Pico, “Impact of grid-forming converters on distance elements based on the X and M calculations,” in *2024 IEEE Texas Power and Energy Conference (TPEC)*. IEEE, 2024, pp. 1–6.

[11] W. W. Baker, “Control, modeling, and analysis of inverter-based resources,” Ph.D. dissertation, Auburn University, 2021.

[12] R. Rosso, S. Engelken, and M. Liserre, “On the implementation of an FRT strategy for grid-forming converters under symmetrical and asymmetrical grid faults,” *IEEE Transactions on Industry Applications*, vol. 57, no. 5, pp. 4385–4397, 2021.

[13] E. Stokes-Waller, “Distance protection: pushing the envelope,” in *Southern African Power System Protection Conference*, 2000, p. 10.